Petroleum Science 20 (2023) 1874–1884

Contents lists available at ScienceDirect

Petroleum Science

journal homepage: www.keaipublishing.com/en/journals/petroleum-science

Original Paper

Three-dimensional dynamics of a single bubble rising near a vertical wall: Paths and wakes

Hong-Jie Yan [a], He-Yang Zhang [a], Hui-Min Zhang [a], Yi-Xiang Liao [b], Liu Liu [a, *]

[a] School of Energy Science and Engineering, Central South University, Changsha, 410083, PR China
[b] Institute of Fluid Dynamics, Helmholtz-Zentrum Dresden-Rossendorf, D-01328, Dresden, Germany

ARTICLE INFO

Article history:
Received 10 November 2022
Received in revised form
16 February 2023
Accepted 16 February 2023
Available online 18 February 2023

Edited by Xiu-Qiu Peng

Keywords:
Bubble
Wall effect
Trajectory
Wake structure
VOF
Basilisk

ABSTRACT

In order to clarify the migration mechanism and wake behavior of a single bubble rising near a vertical wall, three-dimensional direct numerical simulations are implemented based on the open-source software Basilisk and various types of migration paths like linear, zigzag and spiral are investigated. The volume of fluid (VOF) method is used to capture the bubble interface at a small scale, while the gas-liquid interface and high-velocity-gradient regions in the flow field are encrypted with the adaptive mesh refinement technology. The results show that the vertical wall has an obstructive effect on the diffusion of the vortex boundary layer on the surface of the bubble migrating in a straight line, and the resulting reaction force tends to push the bubbles away from the wall surface. For the zigzag or spiral movement of a bubble in the *x-y* plane, the perpendicular wall is an unstable factor, but on the contrary, the motion in the *z-y* plane is stabilized.

1. Introduction

Bubble rising characteristics have always been a research hotspot in the field of two-phase flow (Pang and Wei, 2011; Yan et al., 2022a,b; Zhan et al., 2022). In the oil and gas drilling process, gas invasion can easily lead to overflow, kick, blowout and other security risks if controlled improperly (Sun et al., 2018; Ju et al., 2022). The rising motion of bubbles in annulus fluid is very important for the design of underbalanced drilling.

In recent years, great progress has been made in the theoretical analysis (Sugiyama and Takemura, 2010; Tomiyama et al., 1993), experimental research (Zenit and Magnaudet, 2008; Liu et al., 2015, 2016; Jeong and Park, 2015) and numerical simulation (Antepara et al., 2019; Zhang et al., 2020) of the single bubble rising process. Clift et al. (2005) studied the shape change of bubbles with different parameters as they ascended in liquid, and showed that the ascending trajectory is directly related to the size and deformation of the bubbles. Cano-Lozano et al. (2016) simulated bubbles in the transition region with the trajectory varying from straight to oscillating and summarized three typical regimes including rectilinear axisymmetric, planar zigzagging and spiraling. With the increase of Reynolds number, the ascending trajectory of bubbles presents a complex transformation, which is called the instability of bubble path (Zenit and Magnaudet, 2008). The appearance of the oscillatory path is closely related to the evolution of the wake vortex.

Most of the previous research focused on the migration of wall-free bubbles (De Vries et al., 2002; Mougin and Magnaudet, 2006; Zhang and Ni, 2014; Zhang and Ni, 2017). However, near-wall bubbles exist widely in nature and industrial production (Takemura et al., 2002). Due to the combined action of gravity, inertial force, viscous force, surface tension, as well as the influence of wall effects, the migration law of near-wall bubbles is very complicated (Feng and Bolotnov, 2018; Yan et al., 2022a, b). The motion characteristics of the bubbles are largely affected by the interactions between the bubbles and the walls. The coupling of wall effects and wake instability leads to more complex shape changes and migration paths during bubble ascent.

When the bubble migrates near a vertical wall, the flow field is significantly altered. On the one hand, the existence of solid walls will contribute to an asymmetric flow field distribution around the bubble and the force between the gas-liquid phase will change,

* Corresponding author.
E-mail address: l.liu@csu.edu.cn (L. Liu).

https://doi.org/10.1016/j.petsci.2023.02.014

causing the bubble to move laterally (Hosokawa et al., 2002; Sugioka and Tsukada, 2015). On the other hand, the obstructive effect of the wall makes the wake vortex structure after the bubble more complex (Lee and Park, 2017), resulting in the instability of the boundary layer and the variation of the bubble rising behavior. The coupling effect between the bubble's trajectory, wake structure and vertical wall requires further study. An in-depth analysis of the near-wall bubble buoyancy law, the vortex development, dynamic evolvement and dissipation mechanism in the wake is of great academic significance.

Numerical simulations have been becoming one of the most important tools to study the bubble rising process because of the advantages of abundant information on flow fields and unlimited physical conditions. In this paper, three-dimensional numerical simulations of the rising process of wall-free bubble and near-wall bubble are carried out to investigate the coupling effects between the wall, bubble trajectory and wake structure with three different types of migration paths: linear, zigzag and spiral.

2. Numerical methodology

2.1. Volume of fluid method

In order to effectively capture the phase interface, the volume of fluid (VOF) direct numerical simulation method was used to solve the two-phase flow, based on the open-source software Basilisk (Popinet and Basilisk, 2018). The gas-liquid two phases share a set of governing equations, which includes the continuity equation, momentum equation and an advection equation for the evolution of the volume fraction:

$$\frac{\partial \rho}{\partial t}+\nabla\cdot(\rho \boldsymbol{u})=0 \tag{1}$$

$$\rho\left(\frac{\partial \boldsymbol{u}}{\partial t}+\boldsymbol{u}\cdot\nabla\boldsymbol{u}\right)=-\nabla p+\nabla\cdot\left[\mu\left(\nabla\mathbf{u}+\nabla\mathbf{u}^{\mathrm{T}}\right)\right]+\boldsymbol{F}_{\mathrm{S}}+\rho\boldsymbol{g} \tag{2}$$

$$\frac{\partial \alpha}{\partial t}+\boldsymbol{u}\cdot\nabla\alpha=0 \tag{3}$$

where ρ, t, $\boldsymbol{u}$, μ and p represent the density, time, velocity, viscosity and pressure, respectively. $\boldsymbol{g}$ denotes acceleration of gravity, $\boldsymbol{F}_{\mathrm{s}}$ is the surface tension and α is the volume fraction of the primary phase (here liquid). In addition, the density ρ and viscosity μ are weighted by the volume fraction with g and l subscripts denoting the gas and liquid phase, respectively.

$$\rho=\rho_l\alpha+\rho_g(1-\alpha) \tag{4}$$

$$\mu=\mu_l\alpha+\mu_g(1-\alpha) \tag{5}$$

In the VOF model, the accurate calculation of the surface tension F_{s} is the key to ensure the reliability of the simulation results, and the precise estimation of the interface curvature κ is very important for the performance of the surface tension model.

$$F_{\mathrm{s}}=\sigma\kappa\nabla\alpha \tag{6}$$

where σ represents the coefficient of the surface tension. κ represents the interface curvature.

Here, the height function (Torrey et al., 1985) $h(x,y)$ is adopted to improve the accuracy of curvature calculation, which has been widely used in literature (Owkes et al., 2018; Liu et al., 2022). In order to describe the surface as a graph of a function, a local coordinate function $z=f(x,y)$ is introduced in the derivation of the height function and the interface curvature is calculated through finite difference method as follows:

$$h(x,y)=\frac{1}{\Delta x\Delta y}\int_{y-\Delta y/2}^{y+\Delta y/2}\int_{x-\Delta x/2}^{x+\Delta x/2} f(x,y)\mathrm{d}x\mathrm{d}y \tag{7}$$

$$\kappa=-\nabla\cdot\mathbf{n}=\frac{h_{xx}\left(1+h_y^2\right)+h_{yy}\left(1+h_x^2\right)-2h_{xy}h_xh_y}{\left(1+h_x^2+h_y^2\right)^{3/2}} \tag{8}$$

where h_x, h_y and h_{xx}, h_{yy} represent first and second derivatives of the height function.

Four dimensionless parameters are selected to better describe the motion state of the bubble (Churchill, 1989): Eotvos number $Eo=\rho_{\mathrm{l}}gD^2/\sigma$, Galileo number $Ga=\rho_{\mathrm{l}}g^{1/2}D^{3/2}/\mu_{\mathrm{l}}$, density ratio $\rho_{\mathrm{r}}=\rho_{\mathrm{l}}/\rho_{\mathrm{g}}$ and viscosity ratio $\mu_{\mathrm{r}}=\mu_{\mathrm{l}}/\mu_{\mathrm{g}}$. The following variables are turning dimensionless as below:

$$x^*=\frac{x}{D},y^*=\frac{y}{D},z^*=\frac{z}{D},S^*=\frac{S}{D},\boldsymbol{u}^*=\frac{\boldsymbol{u}}{\sqrt{gD}},t^*=\sqrt{\frac{g}{D}}t \tag{9}$$

where D is the bubble diameter. x, y and z denote the corresponding coordinates in the Cartesian coordinate system. S denotes the initial distance from the bubble centroid to the wall. $\boldsymbol{u}$ represents the velocity and t represents the time.

2.2. Solution

One of the difficulties in solving the momentum equation is the coupling of velocity and pressure. To improve the computational efficiency, the second-order projection method (Chorin, 1969) was adopted for time discretization. The convection term was discretized using the Bell-colella-glaz second-order unsplitting upwind scheme (Bell et al., 1987). During the calculation, the Courant number was set to a fixed value 0.8, and the time step adjusted accordingly. As for the discretization of space, the octree grid division method was applied, which refers to subdividing a square cell into 8 sub-cells of equal size, as shown in Fig. 1.

Adaptive mesh refinement (AMR) technology is used to reduce numerical errors (Wang et al., 2004), as shown in Fig. 2. Adaptive grid indicates that the grid size can be continuously adjusted in the iterative process with dense grid in areas with large gradients of physical variables and sparse grid elsewhere (Theodorakakos and Bergeles, 2004). In this study, the mesh is refined at every time step according to the following criteria:

$$\frac{|\boldsymbol{u}|\Delta}{\max(|\boldsymbol{u}|)}<\varepsilon \tag{10}$$

$$|\nabla\alpha|\Delta<\varepsilon \tag{11}$$

where ε is a user-defined threshold. Δ represents the gird size and it should be noted that here the smallest gird size is used. These two criteria lead to mesh refinement at the gas-liquid interface according to the volume fraction gradient and the bubble wake region according to the velocity, which not only realizes the accurate tracking of the bubble interface, but also ensures the mesh resolution at the wake. In this paper, thresholds of 0.001 for Eq. (10) and 0.0001 for Eq. (11) are adopted.

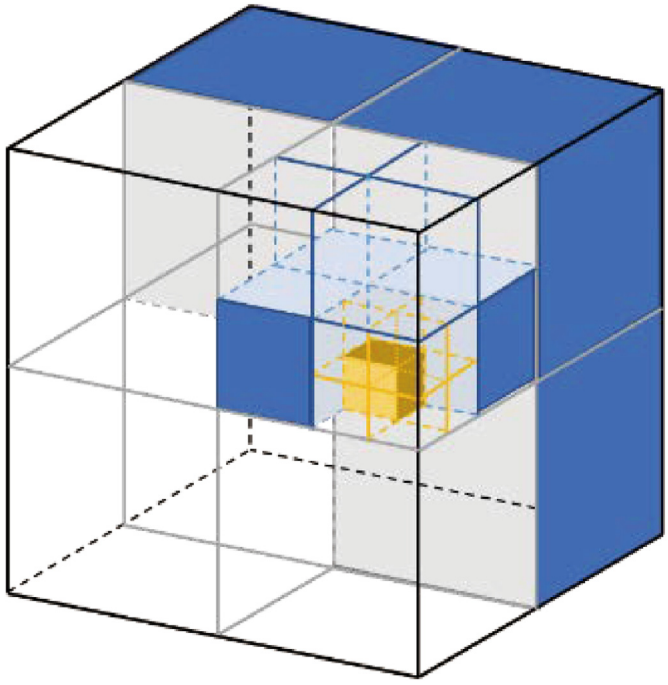

Fig. 1. Schematic diagram of the octree grid.

2.3. Validation

Mesh independence validation was carried out by comparing three levels of mesh refinement, as shown in Table 1. The refinement level indicates the number of times when the grid is encrypted from the coarsest to the smallest. The refined meshes are shown in Fig. 2. The numerical calculation area is $60D \times 60D \times 60D$, and the dimensionless parameters are $Ga = 141.42$, $Eo = 12$, $\rho^* = 0.001$, $\mu^* = 0.01$.

The terminal velocity of different mesh is summarized in Table 1 and the deviation is below 0.5%, which demonstrates the convergence of the computation. The comparison of the trajectory and the velocity are shown in Fig. 3. As the bubble rises, it can be seen that the results of refinement level 11 cannot capture the motion accurately and will cause errors in analysis of the path instability. With refinement level 13, the computation time is 6 times than that of the level 12. Considering both the results accuracy and the computation cost, Mesh2 with refinement level 12 was selected.

In order to verify the performance of the numerical model for the reproduction of the actual situation, a comparison with the experimental data of the near-wall bubble was carried out. The schematic diagram of the experimental device is shown in Fig. 4(a). The rising process of the near-wall bubble was recorded by a high-speed camera, and the characteristics of the bubble (the equivalent diameter, 2-D trajectory, final velocity, etc.) were obtained through image processing. The bubble diameter obtained in the experiment is 2.44 mm. The size of the simulation domain is $147D \times 147D \times 147D$, as shown in Fig. 4(b). The dimensionless distance from the initial position of the bubble centroid to the bottom is 5.6, the dimensionless distance from the initial position to the left wall is 2.559, and the dimensionless parameters are $Ga = 496.19$, $Eo = 0.82$, $\lg Mo = -10.9$. The adaptive mesh refinement is adopted at the bubble interface and the bubble wake.

Table 1
Mesh refinement levels.

Mesh	Refinement at the wake	Refinement at the interface	D/Δ	u^*
Mesh1	5	11	32	0.811
Mesh2	5	12	64	0.814
Mesh3	5	13	128	0.814

Fig. 5(a) and (b) show the comparison of the trajectories and velocity obtained from numerical simulations and experimental tests. It can be seen from Fig. 5 that both the bubble trajectory and velocity are in good agreement. Due to the continuous bubble rotation during the rising process, the bubble movement has a certain randomness, which may be the reason for the error of the bubble trajectory between the experimental test and the numerical simulation. The velocity and frequency of the bubble migration path near the wall are shown in Table 2. The frequency of path in the stable rising stage was obtained by fast Fourier transform. The deviations of the numerical results and experimental data are 0.5% and 5.9% respectively, which are within the acceptable range. Therefore, the established numerical model can accurately capture the near-wall bubble rising process to some extent.

2.4. Physic model and parameters

The physical models of the wall-free bubble and near-wall bubble are shown in Fig. 6. The size of the computational domain is $60D \times 60D \times 60D$. For free bubble, the initial position of the bubble centroid is at the center of the x-z plane and for near-wall bubble the dimensionless distance to the left wall surface is $S = 1$. In both cases the bubble was released $6D$ above the bottom. Different gas-liquid systems are selected according to the different types of bubble trajectories, e.g., the size of the bubble, the physical parameters of the liquid and the surface tension coefficient. The dimensionless parameters for three ascending paths are shown in Table 3.

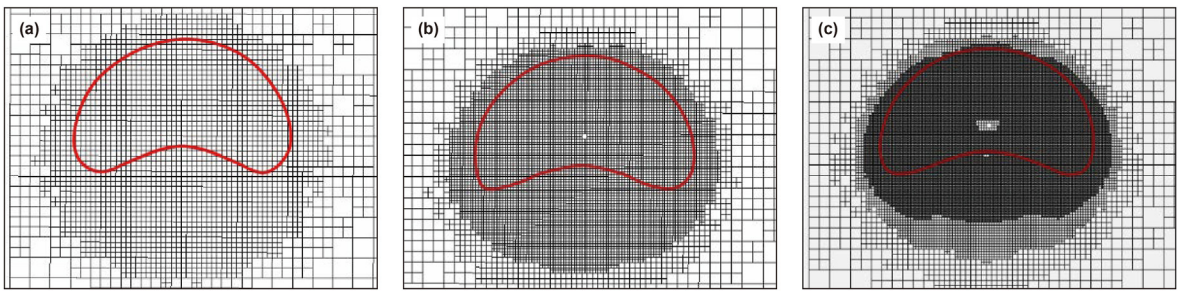

Fig. 2. Schematic diagram of the adaptive mesh refinement. (**a**) Refinement level 11. (**b**) Refinement level 12. (**c**) Refinement level 13.

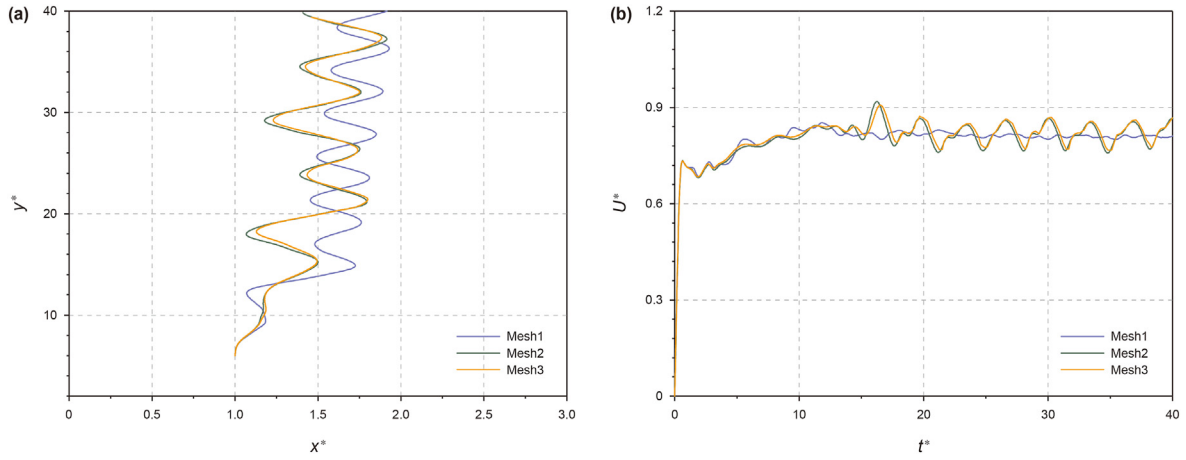

Fig. 3. Comparison of the trajectory and the velocity under different mesh refinement level. (**a**) The trajectory. (**b**) The velocity.

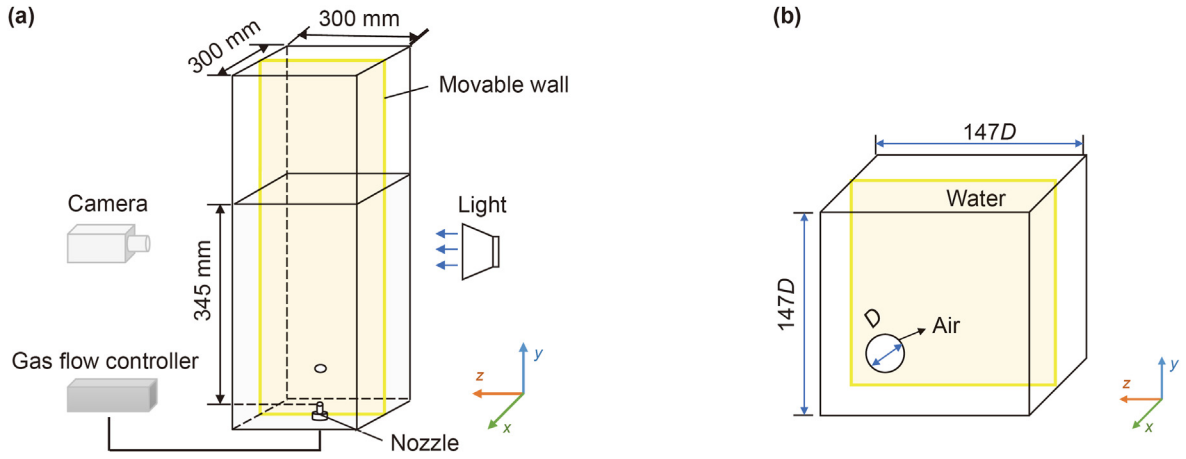

Fig. 4. Schematic diagram of the experimental device and the numerical model. (**a**) The experimental device. (**b**) The numerical model.

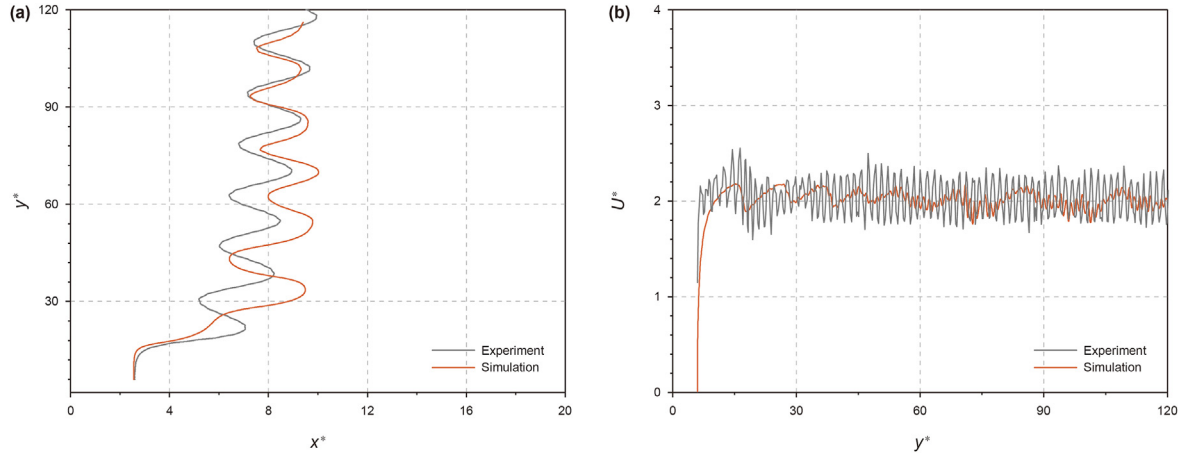

Fig. 5. Comparison between numerical and experimental results. (**a**) Trajectory. (**b**) Velocity.

3. Results and discussions

3.1. Path and wake of the linear motion

Fig. 7 shows the linear path of the bubble from the *x*-*y* plane and *z*-*y* plane, where the horizontal and vertical coordinates represent the horizontal and vertical offsets of the bubble centroid from the initial position, respectively. When the bubble migrates in the approximately unbounded domain, the trajectory of the bubble is almost straight in both directions. When the bubble rises near the

Table 2
Velocity and frequency of bubble near the wall.

	Velocity [-]	Frequency of the trajectory
Experiment	2.02	0.068
Simulation	2.01	0.071
Relative error	0.5%	5.9%

wall to increase gradually, and the trajectory is approximately an oblique line (x-y plane). During the ascent, the bubble gradually moves away from the wall, but the effect becomes weaker with the increase of the distance between the two, and the slope of the migration path became larger.

In the process of bubble rising near the wall, the wall has a

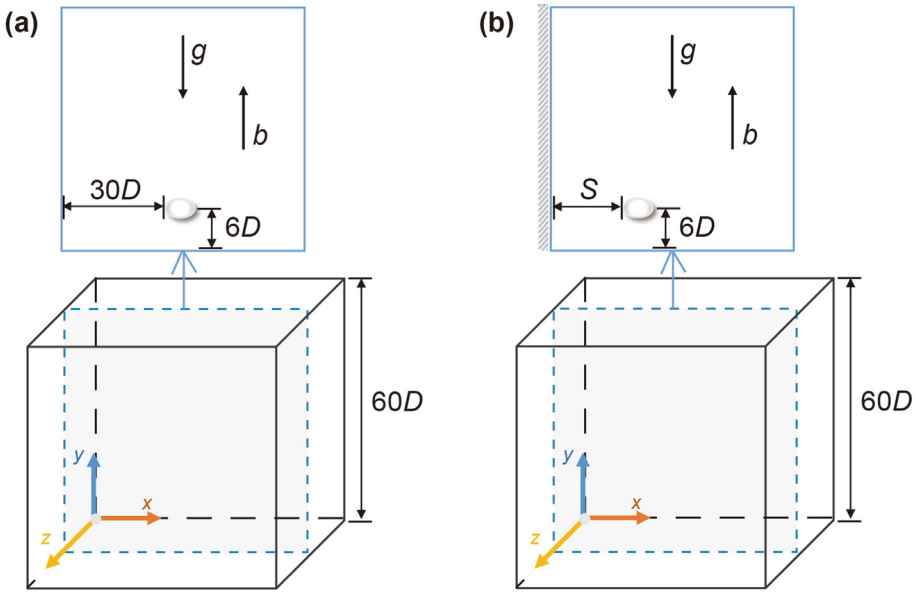

Fig. 6. Physical models. (**a**) The wall-free bubble. (**b**) The near-wall bubble.

Table 3
Dimensionless parameters for simulations.

Path	*Ga*	*Eo*	ρ^*	μ^*
Linear path	8.8	2	0.001	0.01
Zigzag path	141	4	0.001	0.01
Spiral path	141	12	0.001	0.01

hindering effect on the diffusion of the vortex boundary layer on the surface of the bubble. This interaction acts on the bubble and pushes the bubble to move away from the wall, as shown in Fig. 8. The Lambda-2 λ_2 criterion (Jeong and Hussain, 1995) is adopted to capture the plane with the minimal local pressure. The force that drives the bubble away from the wall due to the presence of the

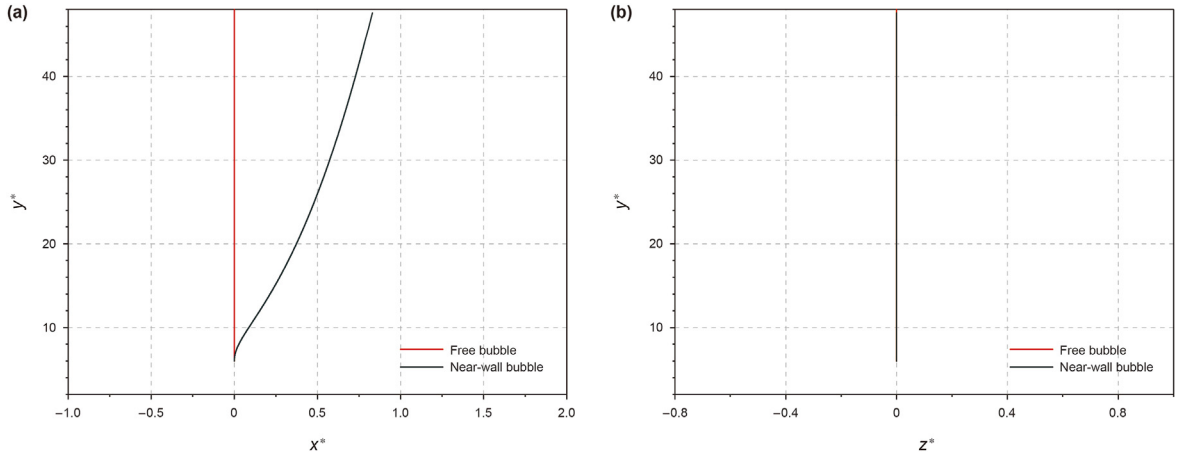

Fig. 7. Linear trajectories of the free bubble and the near-wall bubble. (**a**) x-y plane. (**b**) z-y plane.

wall, the wall effect causes the bubble to migrate laterally on the plane perpendicular to the wall, and the bubble path changes from a 1-*D* linear motion to a 2-*D* migration motion. The existence of the wall causes the horizontal distance between the bubble and the wall is called the wall-induced repulsive lift. Fig. 9 shows the velocity vector distribution around the free bubble and the near-wall bubble. In an unbounded domain, there are symmetrical near-circular vortices on the left and right sides of the bubble, and the

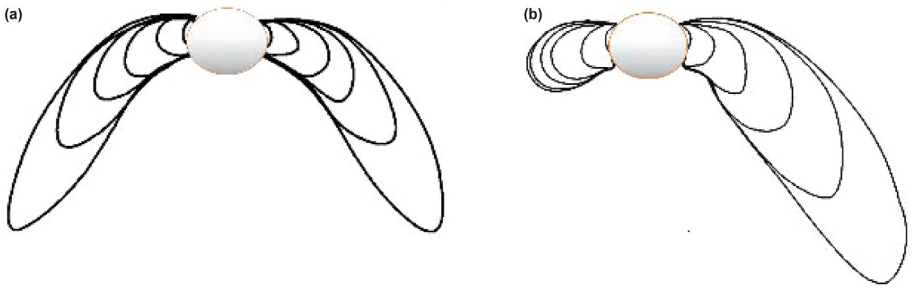

Fig. 8. Vortex structure around the bubble. (**a**) Without the wall. (**b**) Near the wall. (The solid black lines around the bubbles from outside to inside are indicated by $\lambda_2 = -0.01, -0.1, -1, -10, -100, -1000$, respectively.)

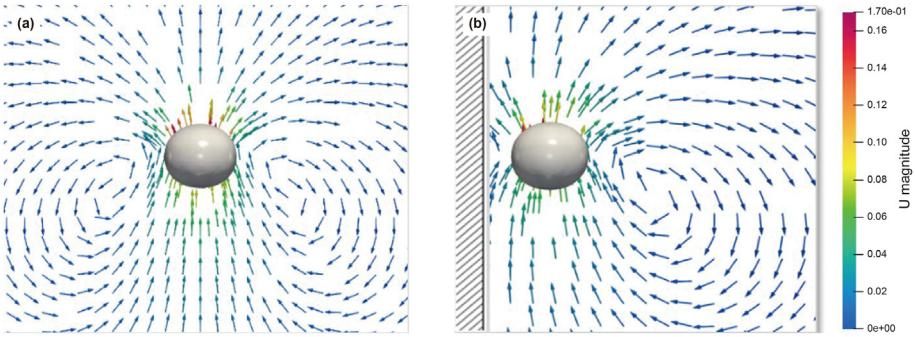

Fig. 9. The velocity vectors near the bubble. (**a**) Without the wall. (**b**) Near the wall.

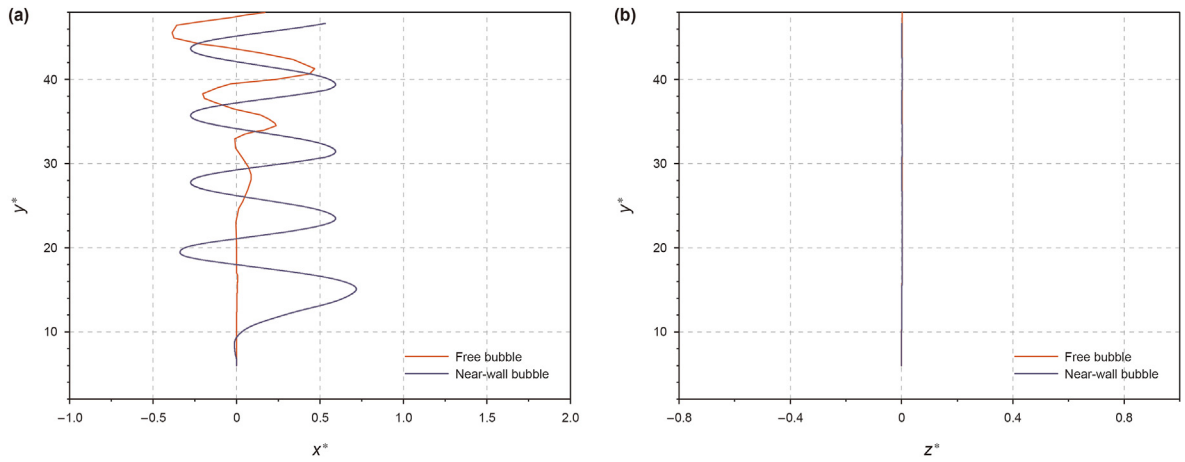

Fig. 10. Zigzag trajectories of the free bubble and the near-wall bubble. (**a**) *x*-*y* plane. (**b**) *z*-*y* plane.

balance of the velocity vector and vortex pair makes the bubble maintain the original linear motion. When the bubble migrates near the vertical wall, the wall restricts the development of the velocity nearby, and the balance of the vortex pair is broken, therefore the bubble moves away from the wall.

3.2. Path and wake of the zigzag motion

Adjusting the dimensionless parameters, the bubble's trajectory changes from one-dimensional linear path to zigzag oscillation, as shown in Fig. 10. When the bubble moves near the wall, the beginning time of bubble oscillation in *x*-*y* plane is obviously advanced, and the migration path is similar to a sine function. The wall has the influence of inducing bubble wakes to fall off, which makes it easier for bubbles to transition from a stable linear upward process to an unstable oscillation state include zigzag and spiral paths. For the zigzag migration, the bubble oscillates only in one direction, while for the spiral migration it shows oscillating motions in both directions.

In the initial stage of bubble rising, the spherical bubble is squeezed into oblate spheres. Fig. 11 shows the shape changes of the free bubble and the near-wall bubble at $t^* = 5$, 10, and 25. At these three moments, the free bubble migrates still along the straight path, and remains symmetric in three directions. When the bubble moves near the wall, because of the wall effects on the flow field distribution around the bubble, the shape of the bubble is no longer symmetrical along the central axis, and the central axis of the bubble also changes from vertical to incline. The deformation of

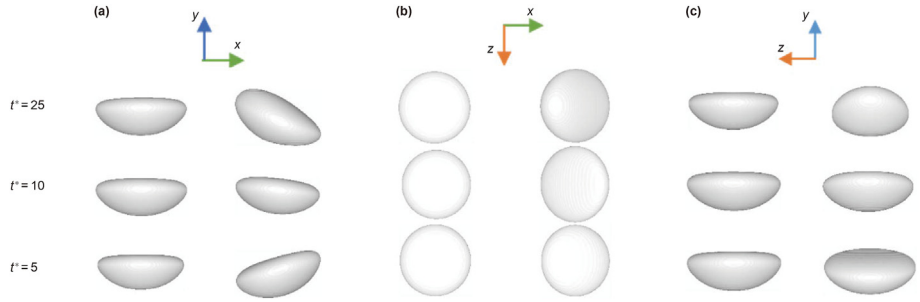

Fig. 11. Three views of the bubble shape at $t^* = 5$, 10, and 25. (**a**) *x-y* plane. (**b**) *x-z* plane. (**c**) *z-y* plane. (The left and right panels of each subgraph correspond to the free bubble and the near-wall bubble, respectively).

the bubble further affects the instability of the migration path. It should be noted that although the bubble loses symmetry in *x* and *y* directions, it still maintains the front and rear plane symmetry in *z* direction. It accords with the zigzag path of bubbles near the wall, when they only oscillate in the *x-y* plane and rise stably in the *z-y* plane.

In general, the vortices can be decomposed into two components: the streamwise vortices and the spanwise vortices. The direction of the streamwise vortices is parallel to the main flow direction. Here the direction of the main flow field is the y-axis direction, therefore $\omega_y = (\partial u/\partial z - \partial w/\partial x)$ is used to describe the streamwise vortices. Fig. 12 shows the streamwise vorticity ω_y of the free bubble at $t^* = 25$. The wall-free bubble still migrates along a straight line without vortex falling off. Meanwhile, the vortex on the near-wall bubble surface falls off periodically during the bubble rising process, as shown in Fig. 13. From the vortex structure after the bubble, it can be concluded that the asymmetric vortices on the *x-y* plane cause bubble's lateral migration. On the *z-y* plane, the vortices are symmetrical leading to a straight path when viewed from the *z-y* plane.

The oscillation of the bubble motion is closely related to the dynamic behavior of the streamwise vortex structure. Studies on free rising bubbles have shown that the appearance of the oscillatory path is caused by the periodic shedding of the wake vortices after the bubble, due to the accumulated streamwise vorticity on the bubble surface exceeding the critical value, which is related to the bubble curvature (Yang and Prosperetti, 2007; Ern et al., 2012). When the bubble migrates near the wall, the shape of the bubble no longer exhibits axis symmetry, and the edges of the bubble become blunt and sharp alternately. The interface curvature on the sharp side of the bubble is larger than that of the free-rising bubble, resulting in early periodic shedding of vortices and the bubble turns into a zigzag path. Fig. 14 presents the horizontal cross-sections of the streamwise vorticity at the downstream after the bubble. Since the strengths of the vortices are only comparable on the *z-y* plane, the bubble rises along the “zigzag” oscillating path.

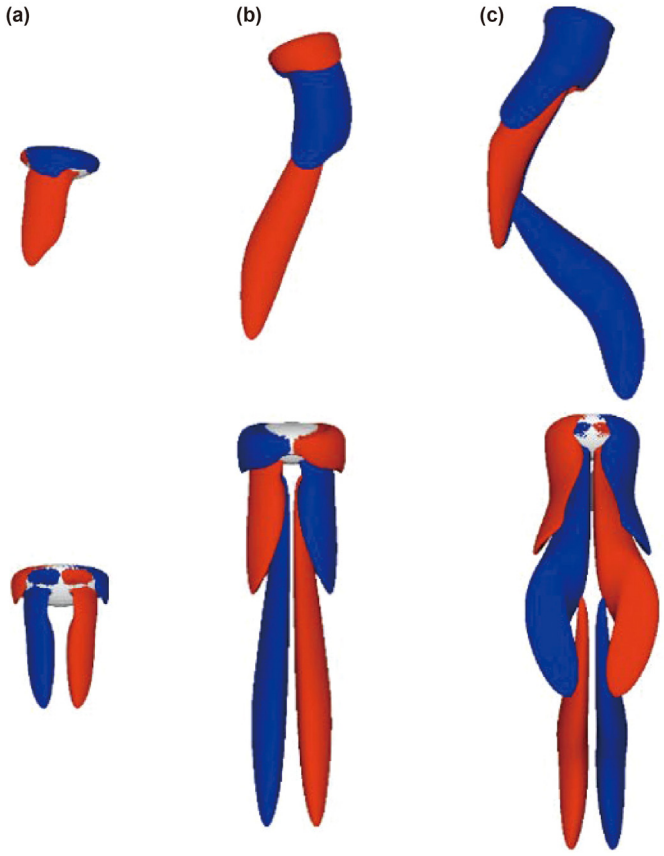

Fig. 13. The vortices evolvement of the near-wall bubble. (**a**) $t^* = 5$. (**b**) $t^* = 10$. (**c**) $t^* = 25$. (The upper is *x-y* plane and the lower is *z-y* plane; $\omega_y = 0.5$ for blue area and $\omega_y = -0.5$ for red area.).

3.3. Path and wake of the spiral motion

Fig. 15 shows the spiral paths of both free bubble and near-wall bubble. The trajectories turn into three-dimensional with the bubble oscillating in both horizontal directions. During the rising process of the free and near-wall bubble, the paths are first linear, then zigzag and spiral in the end. On the *x-y* plane the near-wall bubble starts to oscillate earlier than the free bubble, while on the *z-y* plane almost at the same time but with smaller amplitude. There

Fig. 12. The streamwise vortices structure of the free bubble at $t^* = 25$. (**a**) *x-y* plane. (**b**) *z-y* plane.

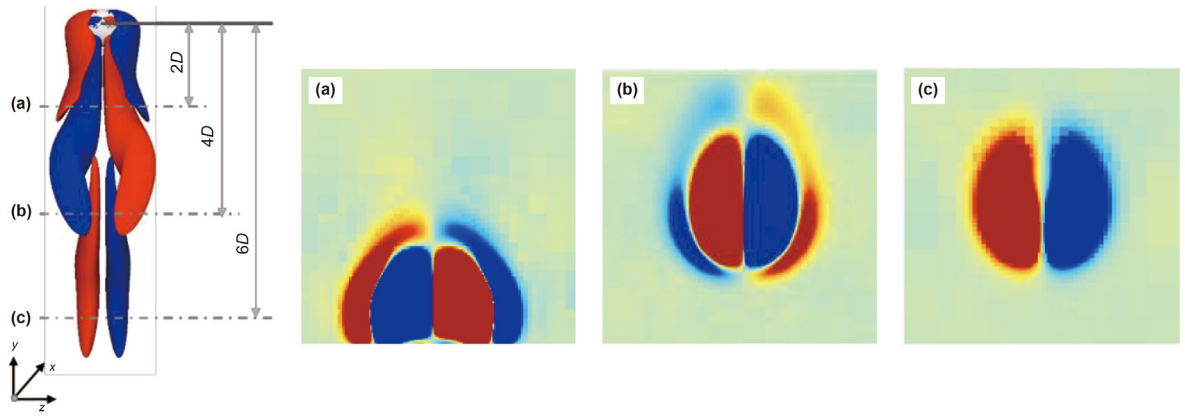

Fig. 14. Horizontal cross-sections of the streamwise vorticity. (**a**) At 2*D* after the bubble. (**b**) At 4*D* after the bubble. (**c**) At 6*D* after the bubble. ($\omega_y = 0.5$ for blue area and $\omega_y = -0.5$ for red area).

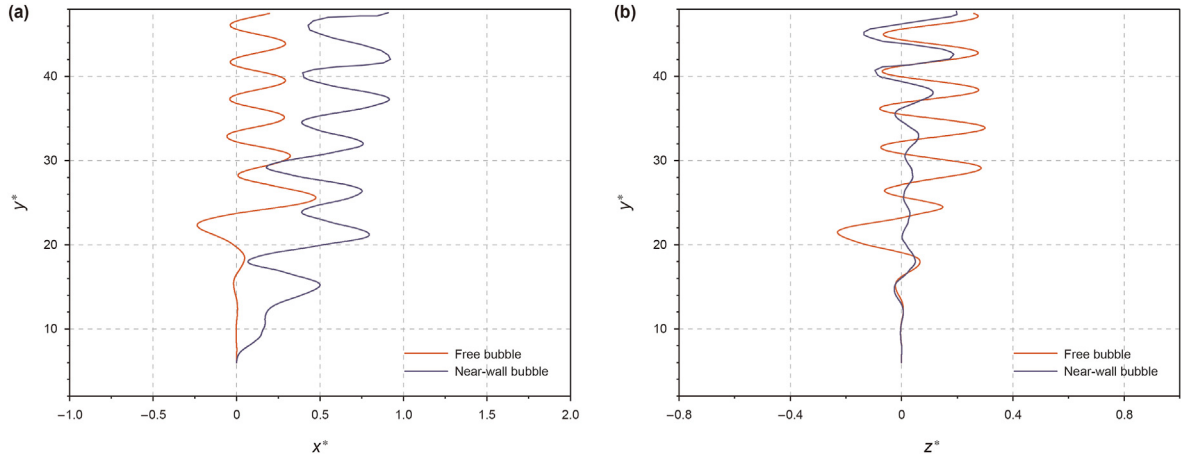

Fig. 15. Spiral trajectories of the free bubble and the near-wall bubble. (**a**) *x*-*y* plane. (**b**) *z*-*y* plane.

Table 4
The amplitudes and frequencies of the free bubble and the near-wall bubble path in different directions.

Type	Plane	Frequency	Amplitude
Free bubble	*x*-*y*	0.229	0.172
	z-*y*	0.229	0.174
Near-wall bubble	*x*-*y*	0.114	0.198
	z-*y*	0.113	0.047

also exists lateral migration away from the wall as observed in the previous cases. Thus, the presence of the wall induces instabilities of the bubble in the direction perpendicular to the wall, while restraining the oscillating motion of the bubble in the direction parallel to the wall. The amplitudes and frequencies of the migration paths in the stable spiral stage obtained by fast Fourier transform are shown in Table 4. For the wall-free bubble, the amplitudes in different directions are basically the same, while when there is a wall the frequency turns smaller meaning a more oscillating path. The amplitudes of the near-wall bubble path shows that the *x*-*y* plane is an unstable factor and the *z*-*y* plane is opposite. The wall has an effect of stabilizing the migration of the bubble on the *z*-*y* plane.

Fig. 16 shows the three-dimensional view of the shape evolution of the free bubble and the near-wall bubble. At $y^* = 10$, the shape of the free bubble still has good symmetry, while the existence of the wall causes the bubble shape to be no longer symmetrical in the *x* direction. As a consequence, the free bubble does not oscillate at this position, and the near-wall bubble only oscillate in the *x* direction. As the bubbles move to $y^* = 16$, the free-rising bubble begins to deform contributing to a slight oscillation in the *z* direction, while the near-wall bubble migrates stably on the *z*-*y* plane with good shape symmetry in the *z* direction. When the height changes to $y^* = 40$, neither of the bubbles remain symmetric shape. A conclusion can be drawn that the migration trajectory is highly related to the change of bubble shape. Fig. 17 compares the shape changes of the near-wall bubble with a zigzag path and a spiral path. The bubble still maintains a certain degree of plane symmetry in the z direction for the zigzag path but loses its symmetry in three directions for the spiral path.

The vortex shedding after the bubble interacts with the shape and migration trajectory of the bubble. The vortex structures at $y^* = 10$, 16 and 40 are shown in Fig. 18, which reveals the reasons for the different upward behaviors of the bubble. The free bubble moves almost along a straight line at the first two positions, and therefore there is no shedding vortex behind the bubbles. When the bubble continues to rise and transition into a spiral path, a pair of counterrotating vortices can be observed after the free and near-wall bubbles. The wake with periodically shedding vortex causes the bubble to oscillate. Different from the zigzag migration bubble, the wake of the bubble at this time is characterized by a pair of fully

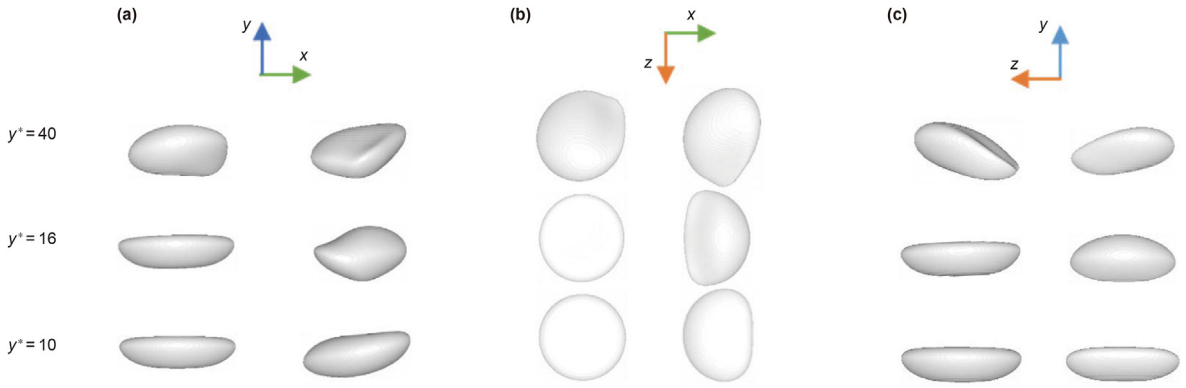

Fig. 16. Three views of the bubble shape at $y^* = 5$, 10, and 25. (**a**) *x*-*y* plane. (**b**) *x*-*z* plane. (**c**) *z*-*y* plane. (The left and right panels of each subgraph correspond to the free bubble and the near-wall bubble respectively).

Fig. 17. Comparison of the near-wall bubble shape from two directions of the *x*-*y* plane. (**a**) With a zigzag path. (**b**) A spiral path.

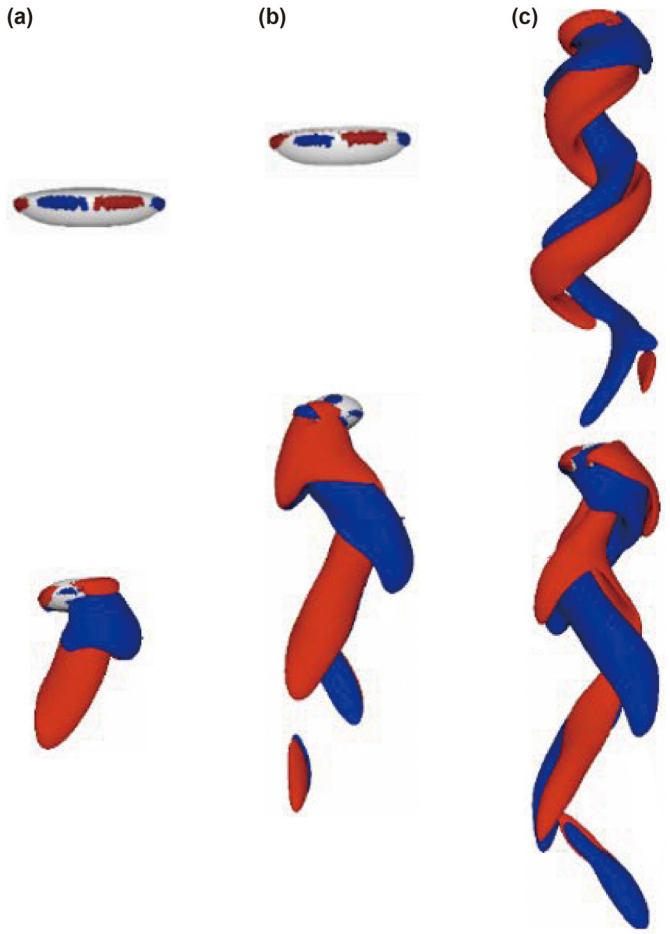

Fig. 18. The vortices evolvement of the near-wall bubble. (**a**) $y^* = 10$. (**b**) $y^* = 16$. (**c**) $y^* = 40$. (The upper is the free bubble and the lower is the near-wall bubble; $\omega_y = 0.5$ for blue area and $\omega_y = -0.5$ for red area).

intertwined flow vortices, and their rotation axis is parallel to the *y* axis. The horizontal cross-sections of the 2*D* far plane downstream of the near-wall bubble is drawn in Fig. 19. The asymmetric deformation of the bubble shape generates the asymmetric vortices pair, and brings about the vortices rotating around the central axis, thereby driving the bubble to spiral motion.

4. Conclusions

In this work, 3-D direct numerical simulations of a single bubble rising with and without a vertical wall (in the y-direction) are performed based on Basilisk. The migration behavior, shape change and wake characteristic of the bubble in linear, zigzag and spiral ascending paths were investigated, and the following conclusions were obtained.

1) The near-wall bubble with linear path will migrate laterally during the rising process. Due to the obstruction of the wall to the diffusion of the vortex, the induced repulsive force pushes the bubble to move away from the wall.
2) For the near-wall bubble with zigzag path, the bubble shape is not fully symmetrical with a counterrotating vortices pair after the bubble. The presence of the wall affects the bubble to oscillate earlier on the *x*-*y* plane turning to a zigzag rising state.
3) When the bubble spirals upward, it oscillates on both *x*-*y* and *z*-*y* planes, and the wake structure becomes a pair of intertwined counterrotating vortices. The wall has a stabilizing effect on the bubble movement on the *z*-*y* plane, resulting in a longer zigzag state during the rising process.
4) The existence of a wall near the bubble has two main effects on the bubble dynamics. One is that the wall changes the flow field distribution around the bubble, which indirectly leads to the lateral migration of the bubble; the other is that the wall induces the wake to fall off, which makes it easier for the bubble to switch from a stable straight state to an unstable oscillation state.

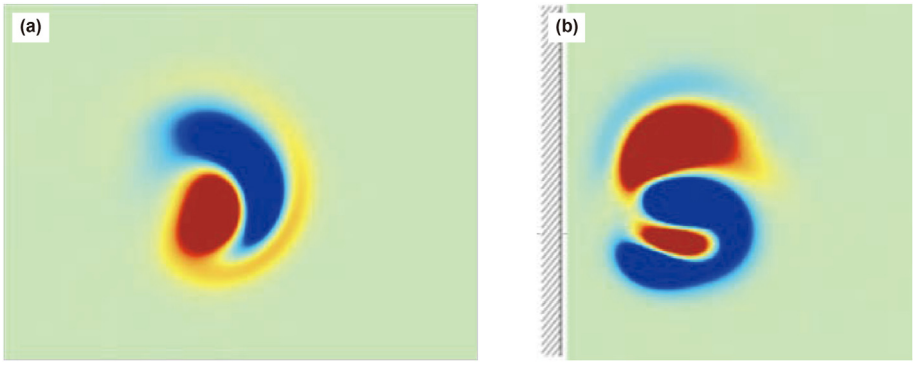

Fig. 19. Horizontal cross-sections of the streamwise vorticity at 2*D*. (**a**) The free bubble. (**b**) The near-wall bubble.

Data availability

The data that support the findings of this study are available from the corresponding author upon reasonable request.

Declaration of competing interest

The authors declare that they have no known competing financial interests or personal relationships that could have appeared to influence the work reported in this paper.

Acknowledgments

This work was supported by the National Natural Science Foundation of China (Grant No. 51906262) and the Hunan Provincial Natural Science Foundation of China (Grant No. 2020JJ5735). The computational resource at the High-Performance Computing Center of Central South University is also gratefully acknowledged.

References

Antepara, O., Balcazar, N., Rigola, J., Oliva, A., 2019. Numerical study of rising bubbles with path instability using conservative level-set and adaptive mesh refinement. J. Computers & Fluids 187, 83–97. https://doi.org/10.1016/j.compfluid.2019.04.013.

Bell, J., Colella, P., Glaz, H., 1987. A second-order projection method for viscous, incompressible flow. J. 8th Computational Fluid Dynamics Conference. 1176, 789–794. https://doi.org/10.2514/6.1987-1176.

Cano-Lozano, J.C., Martinez-Bazan, C., Magnaudet, J., Tchoufag, J., 2016. Paths and wakes of deformable nearly spheroidal rising bubbles close to the transition to path instability. J. Physical Review Fluids 1 (5), 053604. https://doi.org/10.1103/PhysRevFluids.1.053604.

Chorin, A.J., 1969. On the convergence of discrete approximations to the Navier-Stokes equations. J. Mathematics of computation. 23 (106), 341–353. https://doi.org/10.2307/2004428.

Churchill, S.W., 1989. A theoretical structure and correlating equation for the motion of single bubbles. J. Chemical Engineering and Processing: Process Intensif. 26 (3), 269–279. https://doi.org/10.1016/0255-2701(89)80027-3.

Clift, R., Grace, J.R., Weber, M.E., 2005. In: Bubbles, Drops, and Particles, second ed. (Mineola, New York).

De Vries, A.W.G., Biesheuvel, A., Van Wijngaarden, L., 2002. Notes on the path and wake of a gas bubble rising in pure water. J. International journal of multiphase flow 28 (11), 1823–1835. https://doi.org/10.1016/S0301-9322(02)00036-8.

Ern, P., Risso, F., Fabre, D., Magnaudet, J., 2012. Wake-induced oscillatory paths of bodies freely rising or falling in fluids. J. Annual Review of Fluid Mechanics 44 (1), 97–121. https://doi.org/10.1146/annurev-fluid-120710-101250.

Feng, J., Bolotnov, I.A., 2018. Effect of the wall presence on the bubble interfacial forces in a shear flow field. J. International Journal of Multiphase Flow. 99, 73–85. https://doi.org/10.1016/j.ijmultiphaseflow.2017.10.004.

Hosokawa, S., Tomiyama, A., Misaki, S., Hamada, T., January, 2002. Lateral migration of single bubbles due to the presence of wall. J. Fluids Engineering Division Summer Meeting 36150, 855–860. https://doi.org/10.1115/FEDSM2002-31148.

Jeong, H., Park, H., 2015. Near-wall rising behaviour of a deformable bubble at high Reynolds number. J. Journal of Fluid Mechanics 771, 564–594. https://doi.org/10.1017/jfm.2015.191.

Jeong, J., Hussain, F., 1995. On the identification of a vortex. J. Journal of fluid mechanics 285, 69–94. https://doi.org/10.1017/S0022112095000462.

Ju, G.S., Yan, T., Sun, X.F., Qu, J.Y., Hu, Q.B., 2022. Evolution of gas kick and overflow in wellbore and formation pressure inversion method under the condition of failure in well shut-in during a blowout. J. Petroleum Science 19 (2), 678–687. https://doi.org/10.1016/j.petsci.2022.01.004.

Lee, J., Park, H., 2017. Wake structures behind an oscillating bubble rising close to a vertical wall. J. International Journal of Multiphase Flow 91, 225–242. https://doi.org/10.1016/j.ijmultiphaseflow.2017.02.004.

Liu, C., Gao, R., Hu, C., 2022. An approximated volume of fluid method with the modified height function method in the simulation of surface tension driven flows. J. AIP Advances 12, 085308. https://doi.org/10.1063/5.0098717.

Liu, L., Yan, H., Zhao, G., 2015. Experimental studies on the shape and motion of air bubbles in viscous liquids. J. Experimental Thermal and Fluid Science 62, 109–121. https://doi.org/10.1016/j.expthermflusci.2014.11.018.

Liu, L., Yan, H., Zhao, G., Zhuang, J., 2016. Experimental studies on the terminal velocity of air bubbles in water and glycerol aqueous solution. J. Experimental Thermal and Fluid Science. 78, 254–265. https://doi.org/10.1016/j.expthermflusci.2016.06.011.

Mougin, G., Magnaudet, J., 2006. Wake-induced forces and torques on a zigzagging/spiralling bubble. J. Journal of Fluid Mechanics 567, 185–194. https://doi.org/10.1017/S0022112006002266.

Owkes, M., Cauble, E., Senecal, J., Currie, A.R., 2018. Importance of curvature evaluation scale for predictive simulations of dynamic gas–liquid interfaces. J. Comput. Phys. 365, 37–55. https://doi.org/10.1016/j.jcp.2018.03.018.

Pang, M., Wei, J., 2011. Analysis of drag and lift coefficient expressions of bubbly flow system for low to medium Reynolds number. Nucl. Eng. Des. 241, 2204–2213. https://doi.org/10.1016/j.nucengdes.2011.03.046.

Popinet, S., Basilisk, 2018. A free-software program for the solution of partial differential equations on adaptive cartesian meshes. http://basilisk.fr.

Sugioka, K.I., Tsukada, T., 2015. Direct numerical simulations of drag and lift forces acting on a spherical bubble near a plane wall. J. International Journal of Multiphase Flow 71, 32–37. https://doi.org/10.1016/j.ijmultiphaseflow.2014.12.001.

Sugiyama, K., Takemura, F., 2010. On the lateral migration of a slightly deformed bubble rising near a vertical plane wall. J. Journal of fluid mechanics 662, 209–231. https://doi.org/10.1017/S0022112010003149.

Sun, X., Sun, B., Zhang, S., Wang, Z., Gao, Y., Li, H., 2018. A new pattern recognition model for gas kick diagnosis in deepwater drilling. J. Journal of Petroleum Science and Engineering 167, 418–425. https://doi.org/10.1016/j.petrol.2018.04.035.

Takemura, F., Takagi, S., Magnaudet, J., Matsumoto, Y., 2002. Drag and lift forces on a bubble rising near a vertical wall in a viscous liquid. J.. Journal of Fluid Mechanics 461, 277–300. https://doi.org/10.1017/S0022112002008388.

Theodorakakos, A., Bergeles, G., 2004. Simulation of sharp gas–liquid interface using VOF method and adaptive grid local refinement around the interface. J. International Journal for Numerical Methods in Fluids 45 (4), 421–439. https://doi.org/10.1002/fld.706.

Tomiyama, A., Zun, I., Sou, A., Sakaguchi, T., 1993. Numerical analysis of bubble motion with the VOF method. J. Nuclear Engineering and Design 141 (1–2), 69–82. https://doi.org/10.1016/0029-5493(93)90093-O.

Torrey, M.D., Cloutman, L.D., Mjolsness, R.C., Hirt, C.W., 1985. NASA-VOF2D: a computer program for incompressible flows with free surfaces. J. NASA STI/Recon Technical Report N 86, 30116.

Wang, J.P., Borthwick, A.G.L., Taylor, R.E., 2004. Finite-volume-type VOF method on dynamically adaptive quadtree grids. J. International journal for numerical methods in fluids 45 (5), 485–508. https://doi.org/10.1002/fld.712.

Yan, H., Gong, H., Huang, Z., Zhou, P., Liu, L., 2022a. Euler–Euler modeling of reactive bubbly flow in a bubble column. J. Physicals of Fluids. 34 (5), 053306. https://doi.org/10.1063/5.0090952.

Yan, H., Zhang, H., Liao, Y., Zhang, H., Zhou, P., Liu, L., 2022b. A single bubble rising in the vicinity of a vertical wall: a numerical study based on volume of fluid method. J. Ocean Engineering 263, 112379. https://doi.org/10.1016/j.oceaneng.2022.112379.

Yang, B., Prosperetti, A., 2007. Linear stability of the flow past a spheroidal bubble.

J. Journal of Fluid Mechanics. 582, 53–78. https://doi.org/10.1017/S0022112007005691.

Zenit, R., Magnaudet, J., 2008. Path instability of rising spheroidal air bubbles: a shape-controlled process. J. Physics of Fluids. 20 (6), 061702. https://doi.org/10.1063/1.2940368.

Zhan, S., Yuan, R., Huang, Y., Zhang, W., Li, B., Wang, Z., Wang, J., 2022. Numerical simulation of hydrogen bubble growth and mass tansfer on horizontal micro-electrode surface under electrode-normal magnetic field. J. Physics of Fluid. 34 (11), 112120. https://doi.org/10.1063/5.0127299.

Zhang, J., Ni, M.J., 2014. Direct simulation of single bubble motion under vertical magnetic field: paths and wakes. J. Physics of fluids. 26 (10), 102102. https://doi.org/10.1063/1.4896775.

Zhang, J., Ni, M.J., 2017. What happens to the vortex structures when the rising bubble transits from zigzag to spiral. J. Journal of Fluid Mechanics. 828, 353–373. https://doi.org/10.1017/jfm.2017.514.

Zhang, Y., Dabiri, S., Chen, K., You, Y., 2020. An initially spherical bubble rising near a vertical wall. J. International Journal of Heat and Fluid Flow 85, 108649. https://doi.org/10.1016/j.ijheatfluidflow.2020.108649.